
Check for updates

require an explicit downstream boundary condition. We have been developing a one-dimensional (1D) plasma fluid code, where the anisotropic ion pressure (AIP) or the anisotropic ion temperature is directly incorporated in the fluid equations [20–24]. This AIP model enables to make the equation of parallel plasma momentum hyperbolic keeping the finite effect of the parallel viscosity. A virtual divertor (VD) model is used instead of an explicit boundary condition at a sheath entrance. Supersonic plasma flows in a radiative-cooling divertor plasma [21] and in a diverging-magnetic-field divertor plasma [23] were successfully realized. In the present paper, we apply this AIP model to an SXD-like configuration and investigate characteristics of supersonic plasma flow profiles.

## 2. Numerical model

### 2.1. Plasma fluid models

In the AIP model, the parallel and perpendicular components of ion pressure, $p_{i,\parallel}$ and $p_{i,\perp}$, are directly incorporated in the plasma fluid model for inhomogeneous magnetic fields [23,24]. The equations of continuity of ions and parallel plasma momentum are shown below;

$$\frac{\partial n}{\partial t} + B\frac{\partial}{\partial s}\left(\frac{nV}{B}\right) = S, \tag{1}$$

$$\frac{\partial}{\partial t}(m_i nV) + B\frac{\partial}{\partial s}\left[\frac{1}{B}(m_i nV^2 + p_{i,\parallel} + p_e)\right] + \frac{p_{i,\perp} + p_e}{B}\frac{\partial B}{\partial s} = M_m. \tag{2}$$

Eqs. (1) and (2) are solved with those of parallel ion energy, perpendicular ion energy and (isotropic) electron energy which are shown as Eqs. (3)–(5) in Ref. [24] and omitted in this paper. Here, the pressures are defined by $p_\sigma = nT_\sigma$ in which $\sigma$ stands for the species and components as $\sigma \in \{(i, \parallel), (i, \perp), i, e\}$. Note that Eq. (2) is hyperbolic. In the Braginskii equations [16], on the other hand, the equation of parallel plasma momentum is described in terms of the isotropic and anisotropic parts of ion pressure, $p_i \equiv (p_{i,\parallel} + 2p_{i,\perp})/3$ and $\delta p_i \equiv 2(p_{i,\parallel} - p_{i,\perp})/3$ as follows;

$$\frac{\partial}{\partial t}(m_i nV) + B\frac{\partial}{\partial s}\left(\frac{m_i nV^2}{B}\right) + B^{3/2}\frac{\partial}{\partial s}(B^{-3/2}\delta p_i) = -\frac{\partial}{\partial s}(p_i + p_e) + M_m, \tag{3}$$

which is mathematically equivalent to Eq. (2). The anisotropic part $\delta p_i$ in Eq. (3) is approximated by a parallel viscous flux, $\delta p_i \approx -\eta_\parallel B^{-1/2}\partial_s(B^{1/2}V)$, making this equation parabolic. The B2 code [25], which is based on the Braginskii equations, is also partly used for comparisons with the AIP model. The notations of variables and the calculation conditions concerning these two models are the same as Ref. [24] except for boundary conditions of the plasma flow velocity at the sheath entrance used in the B2 code which are described in detail in Section 3.3. The plasma sound speed is defined by $c_s \equiv \sqrt{(T_{i,\parallel} + T_e)/m_i}$ in the AIP model and $c_s \equiv \sqrt{(T_i + T_e)/m_i}$ in the B2 code, respectively.

### 2.2. SXD-like configuration

Fig. 1(a) shows the parallel-to-**B** (the coordinate of which is denoted by $s$) profiles of the magnetic-field strength $B$ and corresponding cross-sectional area of the flux tube $A$ used in this study which is the same as Ref. [24]. The system length is $L = 2.82$ m. The particle source term is artificially given as $S = S_0 \exp[-20(s/L)^2]$ with $S_0 = 1.11 \times 10^{23}$ /m$^3\cdot$ s as shown in Fig. 1 (b). The heat source terms are given as $Q_i = Q_e = (3/2)T_{in}S$ with the source temperature $T_{in} = 10$ eV and $Q_i$ is isotropically divided into $Q_{i,\parallel} = Q_i/3$ and $Q_{i,\perp} = 2Q_i/3$ for the AIP model. The momentum source $M_m$ is set to be zero. As for the boundary conditions, a mirror symmetric condition (i.e. $\partial_s n = V = \partial_s T = 0$) is imposed at $s = 0$. The target is set at $s = L_t$ and $L_t = L$ for Sections 3.1–3.4. For Section 3.5, $L_t$ is changed in the range of $L/2 \le L_t \le L$. The system has the local maximum of $B$ at $s = 2.39$ m giving a magnetic nozzle structure in front of the target except for when $L_t < 2.39$ m. The VD model [21] is used for $s > L_t$ for the sheath boundary condition at $s = L_t$ in the AIP model while the plasma flow velocity $V$ at $s = L_t$ (denoted by $V_t$) is prescribed in the B2 code in Section 3.3.

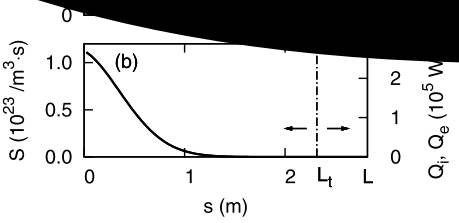


**Fig. 1.** Calculation conditions used in this study; parallel-to-**B** profiles of (a) the magnetic field strength $B$ (solid line), the cross-sectional area of the flux tube $A$ (broken line) and (b) source terms. The vertical chain line represents the target position.

## 3. Results and discussions

### 3.1. Numerical solution from the AIP model

Fig. 2 shows the numerical solution in the steady state obtained from the AIP model. As shown in Fig. 2 (b) and (d), $n \sim 5.88 \times 10^{18}$ /m$^3$ and $T_i \sim 5.48$ eV ($T_{i,\parallel} \sim 5.07$ eV and $T_{i,\perp} \sim 5.69$ eV) are observed at $s = 0$. The mean free path of ion-ion Coulomb collisions is thus evaluated to be m $\ll L$. That is why an almost isotropic $T_i$ is obtained. The Mach number $M \equiv V/c_s$ is comparably low in the upstream diverging magnetic field region and starts to increase in the downstream contracting and diverging magnetic field region (i.e. a magnetic nozzle) as shown in Fig. 2 (c). By assuming that $V \approx 0$, $T_{i,\parallel} \approx T_{i,\perp}$ and $T_{i(e)} \approx$ const. in Eq. (2), $n \approx$ const. is obtained. This is why $n$ in the upstream diverging magnetic field region seems to be almost independent of $B$ and $S$ as shown in Fig. 2 (b).

As is done in Ref [19], the right hand side of the following equation is also investigated;

$$(1 - M^2)\frac{dM}{ds} = \frac{1 + M^2}{nc_s}S + \frac{M(1 + M^2)}{c_s}\frac{dc_s}{ds} + \frac{\tilde{c}_s^2}{c_s^2}\frac{M}{B}\frac{dB}{ds}. \tag{4}$$

This equation describes the parallel gradient of $M$ in the steady state which is obtained by combining Eqs. (1) and (2). Here, $\tilde{c}_s \equiv \sqrt{(T_{i,\perp} + T_e)/m_i}$ is defined for convenience although $\tilde{c}_s^2/c_s^2 \approx 1$ holds due to the isotropy of $T_i$. Eq. (4) tells that the right hand side needs to change its sign from positive to negative at the sonic-transition point $s_{trans}$ so that the plasma flow can continuously transfer from subsonic to supersonic. In Fig. 2 (f), a bifurcation of solutions concerning $s_{trans}$ is observed; $s \sim 0.51$ m at which the effect of $S$ becomes weak enough to balance with that of the diverging magnetic field in Eq. (4) and $s \sim 2.33$ m at which the effect of the contracting magnetic field becomes weak enough to balance with that of the sound-speed gradient term in Eq. (4). If the former became $s_{trans}$, the plasma would not satisfy the Bohm criterion due to the region of the contracting magnetic field. Thus, the plasma chooses the latter as $s_{trans}$ in this case as shown in Fig. 2 (c). The plasma flow transfers from subsonic to supersonic due to the magnetic nozzle effect. The Mach number at the sheath entrance becomes $M_t \sim 2.13$. This tendency of $M$ profile is similar to the experimental result of a linear device [14].

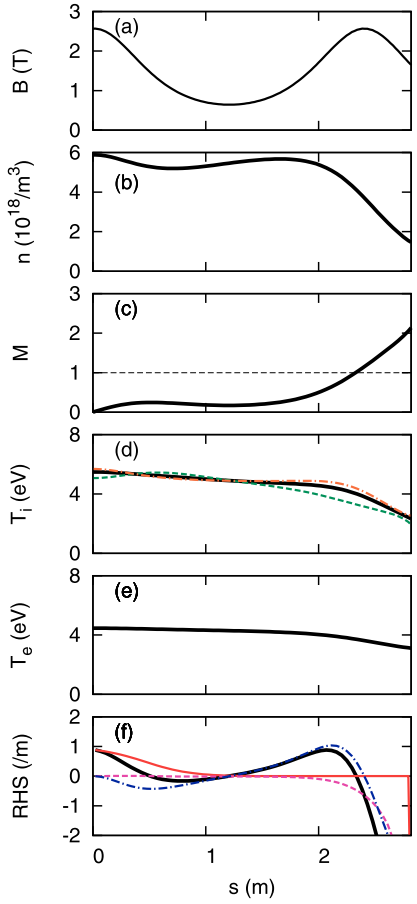


**Fig. 2.** Solution from the AIP model; (a) the magnetic field strength $B$, (b) plasma density $n$, (c) Mach number $M$, (d) effective isotropic ion temperature $T_i \equiv (T_{i,\parallel} + 2T_{i,\perp})/3$ (thick solid line) with parallel $T_{i,\parallel}$ (thin broken line) and perpendicular $T_{i,\perp}$ (thin chain line) components, (e) electron temperature $T_e$ and (f) the right hand side of Eq. (4) (thick solid line) with the first, (thin solid line), the second (thin broken line) and the third (thin chain line) terms of it.

### 3.2. Comparison with an analytical solution

In this section, only are Eqs. (1) and (2) solved under a condition of $T_i = 0$ (i.e. the ions are monoenergetic) and $T_e = 5$ eV in order to compare the solution with an analytical one. The Mach number $M$ profile numerically obtained from the AIP model is shown in Fig. 3. Here, $B_0$ is the magnetic field strength at $s = 0$ and 2.39 m (i.e. the local maximum of $B$). The ions are accelerated in the magnetic nozzle and a supersonic plasma flow is obtained with the sonic-transition point $s_{trans}$ located at the local maximum of $B$ (i.e. $\partial_s B = 0$).

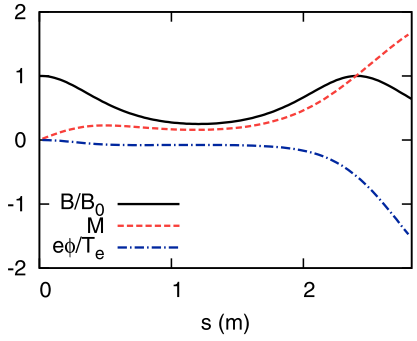


**Fig. 3.** Profiles of normalized magnetic field strength $B/B_0$ (solid line), Mach number $M$ (broken line) and normalized electrostatic potential $e\phi/T_e$ (chain line) obtained from the AIP model.

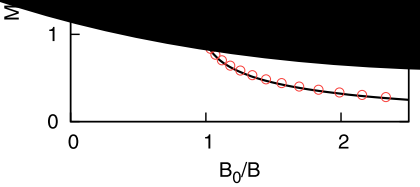


**Fig. 4.** Comparison between an analytical solution (solid line) and one from the AIP model (circles) of the Mach number $M$.

By combining the continuity of ions, $nV/B = \text{const.}$, the ion energy conservation, $m_i V^2/2 + e\phi = \text{const.}$ ($\phi$ represents the electrostatic potential), and the Boltzmann relation, $n \propto \exp(e\phi/T_e)$ [13], together with an assumption that $s_{trans}$ is at the local maximum of $B$, the following analytical solution in a sourceless (i.e. $S = 0$) region is obtained;

$$\frac{B_0}{B} = \frac{1}{M}\exp\left(\frac{M^2 - 1}{2}\right). \tag{5}$$

The same analytical solution is also obtained by combining the steady state and sourceless version of Eqs. (1) and (2). Fig. 4 shows a direct comparison between the numerical solution in the $S \approx 0$ region and the analytical one, and a good agreement is obtained. The profile of the normalized electrostatic potential which is inversely calculated from the density profile and the Boltzmann relation is also shown in Fig. 3. It is found that the acceleration of the ions is caused by the ambipolar electric field in this case, which is not immediately clear from Eq. (2). In a finite-$T_i$ case like Fig. 2, the effect of conservation of the magnetic moment also contributes to the acceleration of the plasma flow in the diverging-magnetic-field region. As a future work, this effect of conservation of the magnetic moment in high-$T_i$ plasmas will be studied.

### 3.3. Comparison with B2 solutions

The solution from the AIP model shown in Fig. 2 is compared with that from the B2 code. Because the equation of parallel plasma momentum, Eq. (3), is parabolic, it requires an explicit boundary condition of the plasma flow velocity at a sheath entrance $V_t$. In this study, three kinds of boundary conditions of $V_t$ are examined; (I) $V_t = c_s$ (i.e. the lower limit of the Bohm criterion), (II) $V_t$ set to be the value obtained from the AIP model (i.e. $V_t = V_{t,AIP} \approx 3.31 \times 10^4$ m/s) and (III) $V_t$ set to be the doubled AIP value (i.e. $V_t = 2V_{t,AIP} \approx 6.63 \times 10^4$ m/s).

Fig. 5 shows a direct comparison of solutions between the AIP model and the B2 code. Note that the B2 code uses a staggered grid in which $V$ is evaluated at cell boundaries while the AIP model uses a collocated one and that the parallel grid width ( $\approx 46$ mm) is fine enough to capture the spatial variation of every physical quantity. The profiles of the AIP model and the B2 code with three kinds of boundary conditions agree well with each other in the $M < 1$ region. As for the $M > 1$ region, on the other hand, it is demonstrated that unrealistic plasma flow profiles can be generated in principle depending on the boundary conditions for $V_t$ although it is possible to adjust the profiles to those from the AIP model to some degree by choosing an appropriate $V_t$. That may lead to an overestimation or underestimation of A&M processes in realistic situations. It is also worth noting that the agreement of profiles between the AIP model and the B2 code in the $M < 1$ region is limited to high-collisionality conditions and that qualitative differences appear in low-collisionality conditions even though a viscous flux limit model is activated [24].

### 3.4. Effects of additional particle sources or sinks

Effects of particle sources or sinks in front of the target plate on the

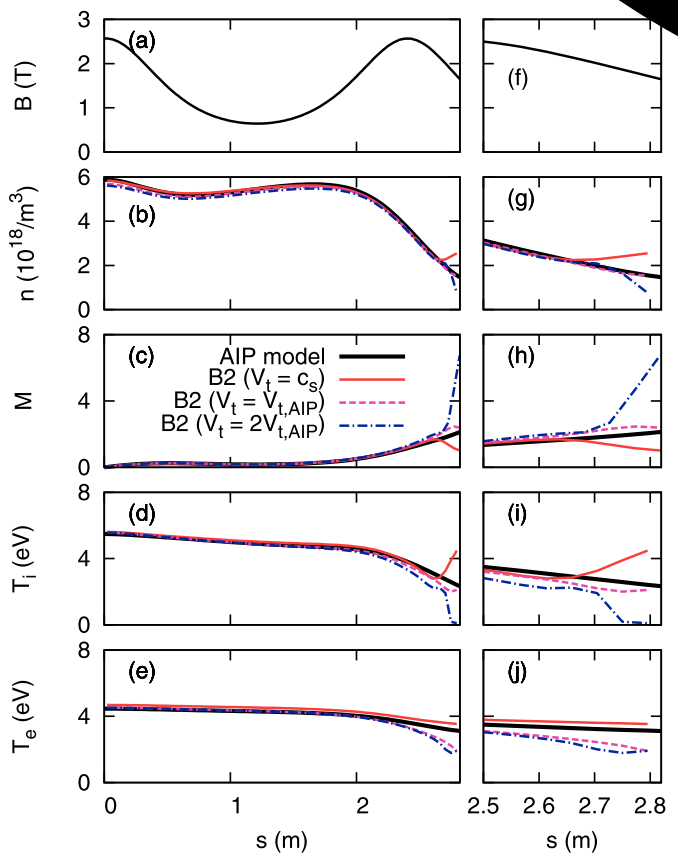


**Fig. 5.** Comparison of solutions from the AIP model (thick solid lines) and the B2 code (thin lines) with different boundary conditions of the plasma flow velocity at the sheath entrance $V_t$; (I) $V_t = c_s$ (thin solid lines), (II) $V_t$ set to be the value obtained from the AIP model (i.e. $V_t = V_{t,AIP} \approx 3.31 \times 10^4$ m/s) (thin broken lines) and (III) $V_t$ set to be the doubled AIP value (i.e. $V_t = 2V_{t,AIP} \approx 6.63 \times 10^4$ m/s) (thin chain lines). Figures (a)-(e) show the magnetic field strength $B$, the plasma density $n$, the Mach number $M$, the ion temperature $T_i$ and the electron temperature $T_e$, respectively. Figures (f)-(j) show enlarged views of (a)–(e).

plasma flow profile are investigated by adding exponential-shape particle sources or sinks in front of the target plate which simply simulate A&M processes given as follows;

$$S = S_{add} \exp\left(\frac{s - L}{\lambda_{add}}\right). \quad (6)$$

Here, $S_{add}$ is chosen from $-0.3S_0 \le S_{add} \le 3S_0$ and $\lambda_{add}$ is fixed at 0.3 m for simplicity. For convenience, the flux amplification $R$ defined as the particle flux at the target normalized by that without additional source or sink (i.e. $S_{add} = 0$) is introduced.

Typical solutions are shown in Fig. 6. As $S_{add}$ becomes larger, $s_{trans}$ moves toward the target plate leading to smaller $M_t$ as shown in Fig. 6 (c) because the effect of the diverging magnetic field in front of the target is more relaxed in Eq. (4) as shown in Fig. 6 (f). If $S_{add} < 0$ is introduced, on the other hand, $s_{trans}$ moves away from the target plate leading to larger $M_t$ as shown in Fig. 6 (c) because the effect of the diverging magnetic field in front of the target is more enhanced in Eq. (4) as shown in Fig. 6 (f). It is hence indicated that a high recycling regime accompanied by a strong particle source region in front of the target may bring about subsonic flows and that plasma detachment regime accompanied by a strong particle sink region in front of the target may lead to supersonic flows. Fig. 7 summarizes $M_t$ as a function of $R$. The reason why $M_t(R)$ is concave up as shown in Fig. 7 is that the coefficient of $S$ in Eq. (4), i.e. $(1 + M^2)/(nc_s)$, decreases as $R$ becomes large due to the increase in $n$ and decrease in $M$ as shown in Fig. 6 (b) and (c).

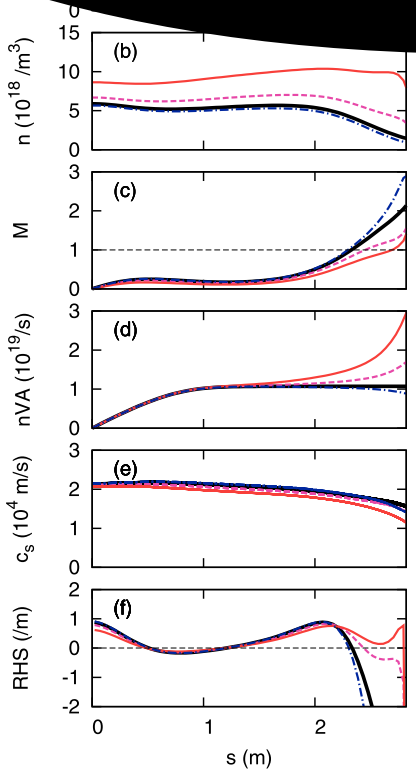


**Fig. 6.** Profiles of (a) $B$, (b) $n$, (c) $M$, (d) the area-integrated particle flux $nVA$, (e) $c_s$ and (f) the right hand side of Eq. (4) for $S_{add}$= 0 (thick solid lines, $R = 1$), $3S_0$ (thin solid lines, $R \sim 2.75$), $S_0$ (thin broken lines, $R \sim 1.58$), $-0.3S_0$ (thin chain lines, $R \sim 0.83$).

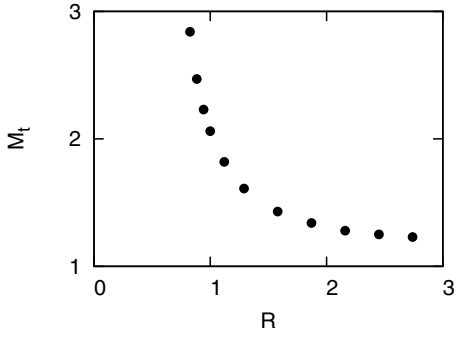


**Fig. 7.** Mach number at the sheath entrance $M_t$ as a function of the flux amplification $R$.

### 3.5. Effects of the target position

The target position $L_t$ is changed in a range of $L/2 \le L_t \le L$ in order to investigate effects of the downstream $B$ profile on the upstream plasma flow profile. Fig. 8 shows typical solutions and the sonic-transition point $s_{trans}$ is summarized as a function of $L_t$ in Fig. 9. Because the temperature is roughly determined by $Q/S \propto T_{in}$ in this case, the $c_s$ profile scarcely changes with $L_t$ as shown in Fig. 8 (d). When the target is located between the original position of $s_{trans} \sim 2.33$ m and $L$, the information of the change in $L_t$ does not propagate upstream and $s_{trans}$ is almost fixed due to the choking of the plasma flow. If the target is in the range of $\sim 1.7$ m $< L_t < 2.33$ m, $s_{trans}$ moves with $L_t$ and, thus, the upstream $M$ profile and corresponding $n$ profile are affected as shown in

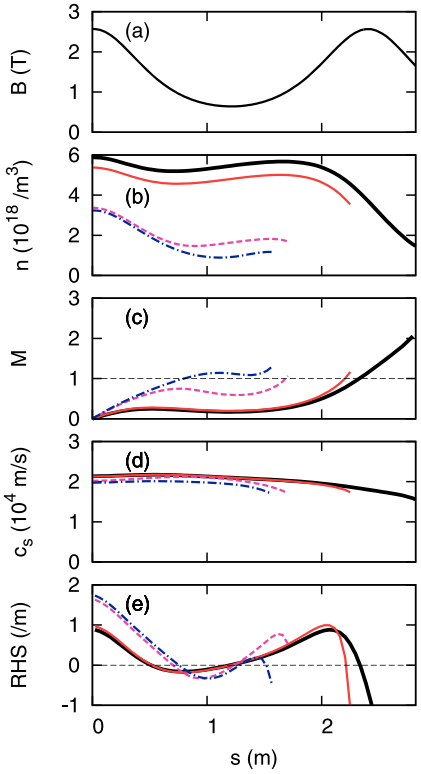


**Fig. 8.** Profiles of (a) $B$, (b) $n$, (c) $M$, (d) $c_s$ and (e) the right hand side of Eq. (4) for $L_t$= 2.82 m (thick solid lines), 2.27 m (thin solid lines), 1.73 m (thin broken lines) and 1.59 m (thin chain lines).

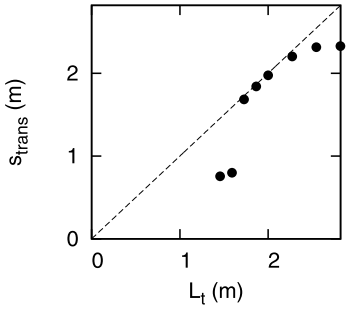


**Fig. 9.** Sonic-transition points $s_{trans}$ as a function of the target position $L_t$.

Fig. 8 (b) and (c). When the target is set above $s \sim 1.7$ m, as shown in Fig. 9, $s_{trans}$ jumps to the other branch discussed in Section 3.1, $s \sim 0.8$ m, because the effect of the downstream contracting magnetic field becomes weak enough as shown in Fig. 8 (e). Therefore, $M$ profile and corresponding $n$ profile are discontinuously changed as shown in Fig. 8 (b) and (c). Such a discontinuous change in $s_{trans}$ and corresponding $M$ profile caused by the bifurcating characteristics of $s_{trans}$ can also be brought about by A&M processes because of the equivalence of $S$ and $dB/ds$ in Eq. (4).

## 4. Summary and future works

An SXD is expected to resolve the issue of rigorous particle and heat loads onto the divertor plates by its total flux expansion. Because of its magnetic-nozzle structure, a self-consistent treatment of supersonic plasma flows can be important in theoretical and numerical studies on the performance of an SXD. The AIP model enables to treat supersonic plasma flows self-consistently by describing the parallel plasma momentum transport with a hyperbolic equation keeping the finite effect of the parallel viscosity. In this study, plasma flow patterns in an SXD-

gener
sonic plasma
profile of the right hand
the Mach number, Eq. (4), shows that the
bifurcation characteristics and that a plasma chooses a proper branch to satisfy the Bohm criterion. Another numerical solution from the AIP model is compared with an analytical one in a case of monoenergetic ions and isothermal electrons and a good agreement is obtained. It also indicates that the acceleration of ions is caused by the ambipolar electric field in this case. Comparison with the Braginskii's plasma fluid model (the B2 code) is also conducted. In the subsonic plasma flow region, the profiles from the AIP model and the B2 code are almost identical due to high collisionality of the plasma. In the supersonic plasma flow region, on the other hand, various unphysical profiles are created by the B2 code depending on the boundary conditions of the plasma flow at the sheath entrance which might lead to an overestimation or underestimation of A&M processes. From a study of effects of additional particle sources or sinks in front of the target, it is found that a particle source/sink in front of the target brings about generations of subsonic/supersonic plasma flow profiles and that $M_t(R)$ becomes concave up. In order to investigate effects of the downstream $B$ profile on the upstream plasma flow profile, the target position is changed. It is found that a discontinuous change in the sonic-transition point and corresponding profile of plasma flow can happen due to the bifurcating characteristics of the sonic-transition point. Such a phenomenon can also be brought about by A&M processes.

In the present paper, an SXD-like configuration is used which is much shorter and simpler compared to realistic SOL-divertor regions of existing or future torus devices. By using this SXD-like configuration, we intended to make the computational time short and to efficiently obtain physical insights on supersonic plasma flows generated by the magnetic nozzle effect. Also, we chose a high-collisionality plasma in this paper because plasma conditions which are more important in an engineering sense such as a high-recycling or a detached plasma are of high collisionality. As future works, simulations on SOL-divertor plasmas of a fusion device incorporating an SXD is planned. Effects of A&M processes on the plasma flow in an SXD will be studied by introducing some neutral models. In addition, effects of supersonic plasma flows on impurity transport and radiation efficiency will be studied.

## Acknowledgments

This work is partly supported by the IEA Technology Collaboration Programme on the Development and Research on Plasma Wall Interaction Facilities for Fusion Reactors (PWI TCP) and the NINS program of Promoting Research by Networking among Institutions (Grant Number 01411702).

## References

[1] P.M. Valanju, et al., Phys. Plasmas 16 (2009) 056110.
[2] D.D. Ryutov, Phys. Plasmas 14 (2007) 064502.
[3] H. Reimerdes, et al., Nucl. Fusion 57 (2017) 126007.
[4] C. Theiler, et al., Nucl. Fusion 57 (2017) 072008.
[5] T. Takimoto, et al., Fusion Eng. Des. 124 (2017) 235–238.
[6] D. Moulton, et al., Plasma Phys. Controlled Fusion 59 (2017) 065011.
[7] M.V. Umansky, et al., Nucl. Mater. Eng. 12 (2017) 918–923.
[8] E. Havlíčková, et al., Plasma Phys. Controlled Fusion 57 (2015) 115001.
[9] T.W. Petrie, et al., Nucl. Fusion 53 (2013) 113024.
[10] B. Lipschultz, F.I. Parra, I.H. Hutchinson, Nucl. Fusion 56 (2016) 056007.
[11] P.C. Stangeby, Modified 2 point model of the SOL to allow for variation in $r_{target}$, http://starfire.utias.utoronto.ca/divimp/publications/2PM-with-R_t-variation-10Aug11-inc.pdf.
[12] R.H. Cohen, D.D. Ryutov, Phys. Plasmas 6 (1999) 1995–2001.
[13] R.H. Cohen, D.D. Ryutov, Contrib. Plasma Phys. 44 (2004) 111–125.
[14] M. Inutake, et al., Arxiv:physics/0410205[physics.plasm-ph].

[15] M. Inutake, et al., J. Plasma Fusion Res. 78 (2002) 1352–1360.
[16] S.I. Braginskii, Rev. Plasma Phys. 1 (1965) 205. Consultants Bureau, New York
[17] O. Marchuk, M.Z. Tokar, J. Comput. Phys. 227 (2007) 1597–1607.
[18] L. Isoardi, et al., J. Comput. Phys. 229 (2010) 2220–2235.
[19] R. Goswami, et al., Phys. Plasmas 21 (2014) 072510.
[20] S. Togo, et al., J. Nucl. Mater. 463 (2015) 502–505.
[25] B.J. Braams,